

## *Supplementary Material*

# **Circumpolar Deep Water impacts glacial meltwater export and coastal biogeochemical cycling along the west Antarctic Peninsula**

Mattias R. Cape<sup>1\*</sup>, Maria Vernet<sup>2</sup>, Erin C. Pettit<sup>3</sup>, Julia Wellner<sup>4</sup>, Martin Truffer<sup>3</sup>, Garrett Akie<sup>5</sup>, Eugene Domack<sup>6</sup>, Amy Leventer<sup>7</sup>, Craig R. Smith<sup>8</sup>, Bruce A. Huber<sup>9</sup>

\* Correspondence: Mattias R. Cape, mcape@uw.edu

## **1 Supplementary Methods**

### **1.1 Water sample analysis method**

#### **1.1.1 Chlorophyll-a**

Water samples for extracted chl-a analysis (50 – 2000 mL) were filtered onto a 25 mm membrane filter (glass fiber filter) and frozen at -80 °C. The filters were then extracted in 90% acetone for 24 hours while stored at -20 °C. Chlorophyll fluorescence was measured using a digital Turner Designs 10-AU fluorometer, calibrated with pure chl-a extracted from *Anacystis nidulans* (Sigma Co.) with concentration measured spectrophotometrically (Jeffrey and Humphrey 1975).

#### **1.1.2 Macro-nutrients**

The phosphate method was a modification of the molybdenum blue procedure of Bernhardt and Wilhelms (1967) in which phosphate was determined as a reduced phosphomolybdic acid employing hydrazine as the reductant. The nitrate + nitrite analysis used the basic method of Armstrong et al. (1967) with modifications to improve the precision and ease of operation. Sulfanilamide and N-(1-Naphthyl) ethylenediamine dihydrochloride reacted with nitrite to form a colored diazo compound. For the nitrate + nitrite analysis, nitrate (NO<sub>3</sub><sup>-</sup>) was first reduced to nitrite (NO<sub>2</sub><sup>-</sup>) using a cadmium reduction column and imidazole buffer as described by Patton. Nitrite analysis was performed on a separate channel, omitting the cadmium reductor. The silicic acid method was based on that of Armstrong et al. (1967) as adapted by Atlas et al. (1971). Addition of an acidic molybdate reagent formed silicomolybdic acid which was then reduced by stannous chloride. Ammonium was determined by a modified indophenol blue method modified from ALPKEM RFA methodology which references Methods for Chemical Analysis of Water and Wastes, March 1984, EPA-600/4-79-020, “Nitrogen Ammonia”, Method 350.1 (Colorimetric, Automated Phenate).

#### **1.1.3 Oxygen isotopes**

Water samples for quantification of oxygen isotopes (δ<sup>18</sup>O) were sealed in glass vials with little head space and were kept chilled with elemental copper until analyzed, following the methods of Rahn and Wetger (2009). The analysis, performed on a Thermo Finnigan Delta V Advantage isotope ratio mass spectrometer, was calibrated against a primary international standard (SMOW1) as well as secondary lab standards (Vostok, B2192 (*Elemental Microanalysis Ltd* “zero natural water”) and distilled water). During analysis, 200 μL of each standard and sample were flushed for 6 min with 0.3% CO<sub>2</sub> in He, then left to equilibrate at 25°C for a minimum of 18h before being analyzed. After sample

equilibration, system suitability and linearity were determined using a CO<sub>2</sub> reference peak. Each sample run included SMOW1 and distilled water check standards after analysis of 5-10 unknown samples. Instrument drift was tracked by analyzing Vostok water at the start and end of each sample run. Three repeated measurements on each unknown sample typically reach a precision better than  $\pm 0.1\text{‰}$ .

## 1.2 Water mass identification, transformation, and analysis

Interactions between the ocean and the ice sheet at the glacial front changes oceanic water masses in characteristic ways (Jenkins 1999). Melting of glacial ice requires the extraction of ocean heat to increase ice temperature to the freezing point and subsequently melt ice. This heat extraction leads to a decrease in temperature of oceanic waters through mixing. The input of subglacial freshwater into the water column also contributes to a concomitant freshening. For a single oceanic water mass interacting with the ice sheet, glacial transformation of ambient waters as a result of submarine melting of a glacier terminus is reflected in  $\Theta$ - $S_A$  space by a shift in seawater properties along a line with a slope of approximately 2.5 °C per salinity unit (i.e., the Gade line, see equation (1) below) connecting oceanic endmember properties with those of submarine melt (Gade 1979; Jenkins 1999). Mixing of ocean waters with subglacial discharge leads to a smaller decrease in temperature (given that the water is at or above the melting point and no phase transition is required) as well as a freshening of fjord water masses. In  $\Theta$ - $S_A$  space, this is reflected in water mass property shifts along a shallower mixing line linking ambient waters to the subglacial discharge endmember (SGD;  $\Theta = -1.8$  °C,  $S_A = 0$  g/kg) (see **Figure 3g**, **Supplementary Figure 2**).

Interactions between ocean waters and glaciers may involve several oceanic water masses (in Barilari, potentially mUCDW, WW, and AASW), with injection of subglacial discharge and export of submarine melt. These interactions lead to transformation of ambient physical and biogeochemical properties as these oceanic waters are not only transformed by glacial interactions but also mixed near the glacial terminus. Upwelling, a result of input of buoyant freshwater, also leads to convective motion which entrains both glacial and ambient water masses towards the surface, redistributing water masses vertically (Jenkins 1999). A water parcel sampled at any given depth within the fjord may therefore be composed of ambient waters from different levels, as well as freshwater exported from the ice sheet.

In interpreting anomalies, we assume that changes in seawater properties are primarily driven by interactions with the glacial ice in Barilari Bay. Within the euphotic zone, atmosphere-ocean interactions, and, in the case of nutrients and oxygen, biological cycling, also impact water mass properties. We return to this point in the discussion below.

## 1.3 Partitioning freshwater concentrations and sources

A number of inverse models, taking advantage of differences in physical and chemical tracer properties of glacial and oceanic water masses, have been employed in the literature to parse out glacial meltwater contributions to an observed seawater mixture (e.g., Beaird et al. 2015; Jenkins 1999; Meredith et al. 2008). These models differ in the way they account for the complexity of ocean structure, as well as melting and mixing processes, resulting in differences in the number of glacial and ambient endmember water types each method resolves and their relative uncertainties. Here we employ three models to constrain water mass distributions and composition.

### 1.3.1 Model 1 – Mor13

Observed temperature and salinity properties of fjord waters are here interpreted as resulting from mixing of mUCDW with subglacial discharge, as well as the submarine melting of the glacier terminus. In practice, the model discretizes these near-simultaneous melting and mixing processes by considering: 1) mixing of mUCDW (with properties  $\Theta_{mUCDW}$ ,  $S_{mUCDW}$ ) with subglacial discharge (SGD;  $\Theta_{SGD} \sim 0$  °C,  $S_{SGD} = 0$  g/kg), resulting in a mixed water mass with properties ( $\Theta'$ ,  $S_A'$ ), and 2) melting of glacial ice, which shifts the properties of this mixed water mass along a melt-line (Gade 1979) with slope:

$$\frac{\partial \Theta}{\partial S_A} = \frac{1}{S_A} \left( \frac{L}{c_p} - \frac{c_i}{c_p} (\Theta_i - \Theta_f) - (\Theta_f - \Theta) \right) \quad (1)$$

Here,  $L$  is the latent heat of fusion,  $c_i$  and  $c_p$  are the heat capacities of ice and seawater, respectively,  $\Theta_i$  is the temperature of glacial ice,  $\Theta_f$  is the freezing temperature, and  $\Theta$ ,  $S_A$  are the temperature and salinity properties of ambient source waters. The result of these processes is the temperature and salinity of the observed water mass ( $(\Theta_{obs}, S_{obs})$ ; **Supplementary Figure 2**).

We utilize temperature and salinity collected from the CTD to parse out contributions by the three water masses. Interaction between mUCDW and a glacier leads to a decrease in salinity proportional to the total freshwater content of the water column ( $f_{FW}$ ):

$$f_{FW} = 1 - f_{mUCDW} = 1 - \frac{S_{A,obs}}{S_{A,mUCDW}} \quad (2)$$

where  $S_{A,obs}$  is the observed salinity of the mixture and  $S_{A,mUCDW}$  is the salinity of the mUCDW endmember (34.69 g/kg). In this model, this total freshwater fraction represents the sum of contributions from subglacial discharge ( $f_{SGD}$ ) and submarine melt ( $f_{SMW}$ ), such that  $f_{FW} = f_{SGD} + f_{SMW}$ . We solve for these individual components using the following scheme.

Observed fjord properties ( $\Theta_{obs}$ ,  $S_{A,obs}$ ) are related to the properties of the mixed water mass ( $\Theta'$ ,  $S_A'$ ) through the melt line ( $\Theta_m$ ,  $S_{A,m}$ ) defined by the Gade slope (equation (1))

$$\Theta_m = \frac{\partial \Theta}{\partial S_A} S_{A,m} + \beta_m = \frac{\partial \Theta}{\partial S_A} S_{A,m} + \left( \Theta_{obs} - \frac{\partial \Theta}{\partial S_A} S_{A,obs} \right) \quad (3)$$

Similarly, the mixing-line linking the properties of mUCDW ( $\Theta_{mUCDW}$ ,  $S_{A,mUCDW}$ ) and those of the subglacial discharge endmember ( $\Theta_{SGD}$ ,  $S_{A,SGD}$ ), and on which the mixed water mass properties also reside (i.e.,  $\Theta'$ ,  $S_A'$ ), is defined by:

$$\Theta' = \frac{\Theta_{mUCDW}}{S_{A,mUCDW}} S' \quad (4)$$

Using equation (3) and (4), we solve for the salinity of the mixed water mass ( $S_A'$ ):

$$S_A' = \left( \Theta_{obs} - \frac{\partial \Theta}{\partial S_A} S_{A,obs} \right) \left( \frac{\Theta_{mUCDW}}{S_{A,mUCDW}} - \frac{\partial \Theta}{\partial S_A} \right)^{-1} \quad (5)$$

The subglacial fraction is then calculated as:

$$f_{SGD} = 1 - \frac{S_A'}{S_{A,mUCDW}} \quad (6)$$

And the fraction of submarine melt as:

$$f_{SMW} = f_{FW} - f_{SGD} \quad (7)$$

See (Mortensen et al., 2013) for the theoretical underpinnings of the method.

### 1.3.2 Model 2 – Jen99

In this model, a composite water mass property, derived from the water column measurement of two conservative properties ( $\chi^1$  and  $\chi^2$ ), is defined as:

$$\psi^{2,1} = (\chi^2 - \chi_{CDW}^2) - (\chi^1 - \chi_{CDW}^1) \left( \frac{\chi_{WW}^2 - \chi_{CDW}^2}{\chi_{WW}^1 - \chi_{CDW}^1} \right) \quad (8)$$

This property, itself conservative, is zero for any mixture of mUCDW and WW. Departures from zero in observations are associated with transformation of ambient waters, in our case as a result of melting of glacial ice. Once these properties have been calculated from observation, meltwater fraction ( $\varphi$ ) can then be computed as

$$\varphi = \frac{\psi_{obs}^{2,1}}{\psi_{melt}^{2,1}} \quad (9)$$

Where  $\psi_{melt}^{2,1}$  refers to the composite property of glacial meltwater.

Meltwater content of fjord waters is effectively limited by the heat content of the water mass in contact with the glacier (Jenkins 1999). Once enough heat has been extracted from the water to depress its temperature to the *in situ* freezing point, no additional melting can occur. An upper limit on the meltwater fraction is given by

$$\varphi \leq \left[ 1 + \frac{L + c_i(\theta_f - \theta_i)}{c_p(\theta - \theta_f)} \right]^{-1} \quad (10)$$

With variables as listed in equation (1). For an ambient water temperature of  $\Theta=0.92$  °C, this corresponds to a maximum meltwater fraction of approximately 3%. We denote this upper limit in figures when reporting meltwater concentrations.

While any two conservative properties can be used in this computation, only those pairs for which the ambient trend (line linking properties of WW and mUCDW) and meltwater mixing lines do not significantly overlap produce determinate meltwater fractions. In our case, these lines overlap in  $\Theta$ - $S_A$ ,  $\delta^{18}\text{O}$ - $S_A$  and  $\delta^{18}\text{O}$ - $\Theta$  spaces (e.g. **Figure 5b**), prohibiting conclusive discrimination of glacial meltwater from the contributions of ambient waters. Instead, we use CTD-derived dissolved oxygen (DO) and salinity, which show clearer separation between fjord profiles and those at reference stations (**Figure 6a**).

While this model does not account for the export of freshwater as subglacial discharge to the marine environment, examination of the resulting observationally-derived meltwater fractions, in the context of theory, can yield insight into where other sources of freshwater (e.g. runoff, sea ice melt) may be important.

### 1.3.3 Model 3 – Mer08

Mer08 determines contribution of sea ice melt, meteoric water, and mUCDW to a mixture by solving:

$$\begin{bmatrix} \delta_{sim} & \delta_{met} & \delta_{mUCDW} \\ S_{A,sim} & S_{A,met} & S_{A,mUCDW} \\ 1 & 1 & 1 \end{bmatrix} \begin{bmatrix} f_{sim} \\ f_{met} \\ f_{mUCDW} \end{bmatrix} = \begin{bmatrix} \delta_{obs} \\ S_{A,obs} \\ 1 \end{bmatrix} \quad (11)$$

Where  $\delta_{sim}$ ,  $\delta_{met}$ , and  $\delta_{mUCDW}$  are the endmember  $\delta^{18}\text{O}$  properties,  $S_{A,sim}$ ,  $S_{A,met}$ , and  $S_{A,mUCDW}$  are the endmember salinity properties,  $f_{sim}$ ,  $f_{met}$ , and  $f_{mUCDW}$  are the endmember fractions, and  $\delta_{obs}$  and  $S_{A,obs}$  are observed properties of the ambient water column at a particular sampling location. We point out that like Mor13, this method considers a single ambient water mass, mUCDW.

### 1.3.4 Model parametrization and assumptions

Tracers and parameters used in these models are shown in **Supplementary Table 1**. We use glacial endmember properties defined by Jenkins and Jacobs (2008), given similarities in the physical setting, with the exception of  $\delta_{met}$ , which we derive from average  $\delta^{18}\text{O}$  property of glacial ice collected in Brialmont Cove during the cruise (see above). We use sea ice properties from Meredith et al., (2008) for the Mer08 model. Local ocean endmember properties are in turn derived from hydrographic profiles at the reference stations. We note that these models assume a closed system in which only interactions with the glacier, and subsequent mixing within the fjord, lead to water mass transformation, along with sea ice formation / melting and precipitation into the ocean in the case of Jen99. For Mor13 and Jen99, this assumption is violated at the ocean surface, where solar insolation, biological growth, and gas exchange can impact water mass properties independently of glacial or sea ice modification. We therefore note both mixed layer depth and euphotic zone depths, and account for these potential sources of modification in reporting and discussing results.

## 1.4 Ice flux delivery

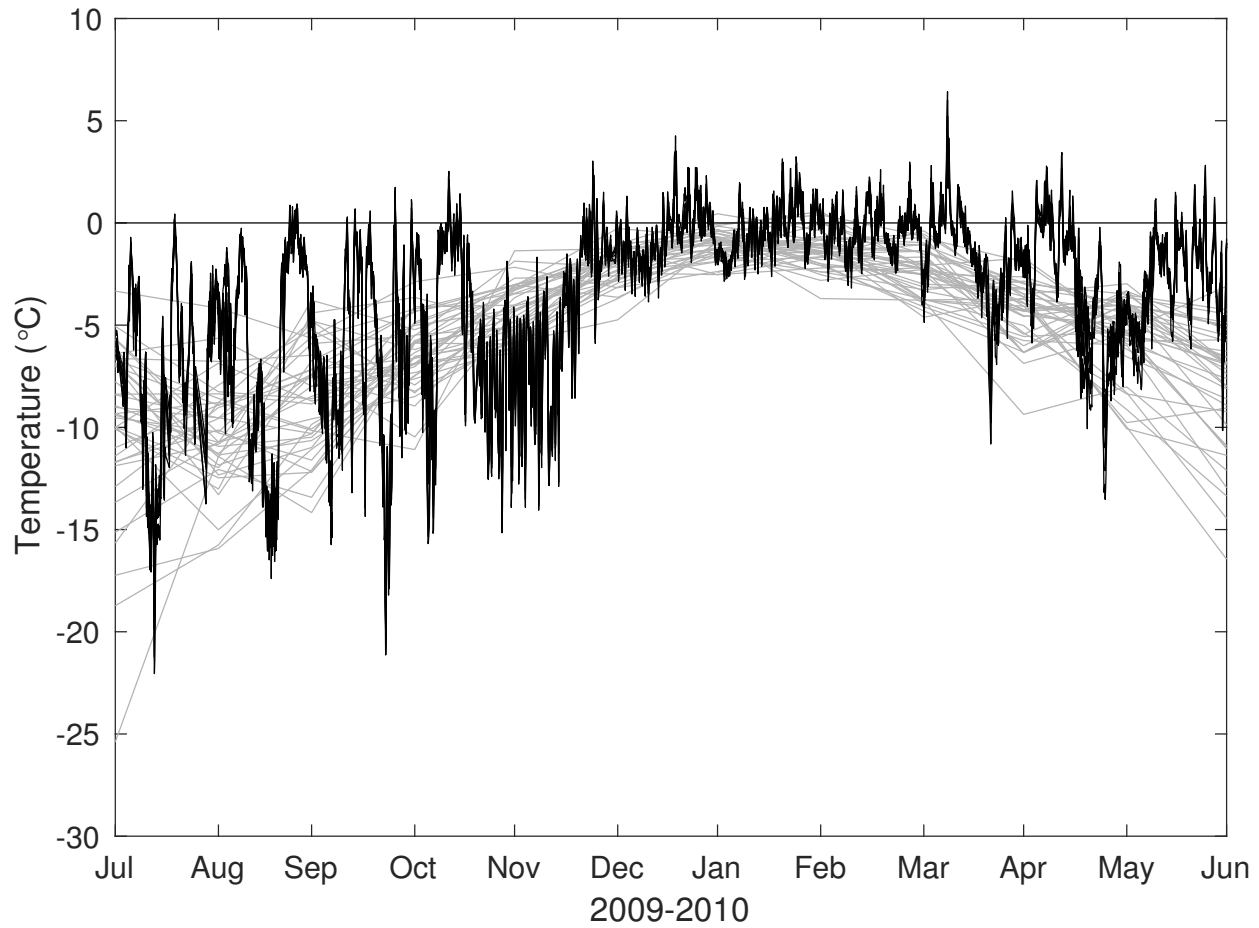
Ice flux calculation for ice delivery into the fjords is derived from the balance flux model of Budd and Warner, 1996, implemented numerically in a similar way to Xiaolan and Jezek, 2004. For the purposes of this study, we assume steady state, that ice flow direction is defined by modern surface topography (DEM from Cook et al., 2012), and we calculate ice flux and delivery to the ocean through each glacier flowing into Barilari Bay (grounding lines based on MOA2009, Haran et al., 2014). Specifically, in the model, we assume that the net precipitation (predominantly precipitation as snowfall) entering the glacierized region moves downhill from grid cell to grid cell along steepest path and ultimately must be balanced by ablation (for Barilari Bay this is dominated by calving and melt at the terminus). The gridded precipitation is derived from surface mass balance predicted by RACMO2 model with a 5.5 km grid cell from a 30-year average 1979 to 2013 (van Wessem et al., 2016) and downscaled to the model grid; some error derives from 5.5km grid cells that are larger than topographic features controlling ice flow. The DEM (Cook et al., 2012) was minimally smoothed and processed to remove holes and stabilize the model calculations. Importantly, we do not include any parameterize for ice flow dynamics. This assumption leads to an artificial narrowing of

the ice discharge to the central band of each glacier by subtleties of the DEM. These results are sufficient for determining glacier mean discharge across a transect (flux-gate method), but not for spatial pattern of discharge within a single glacier.

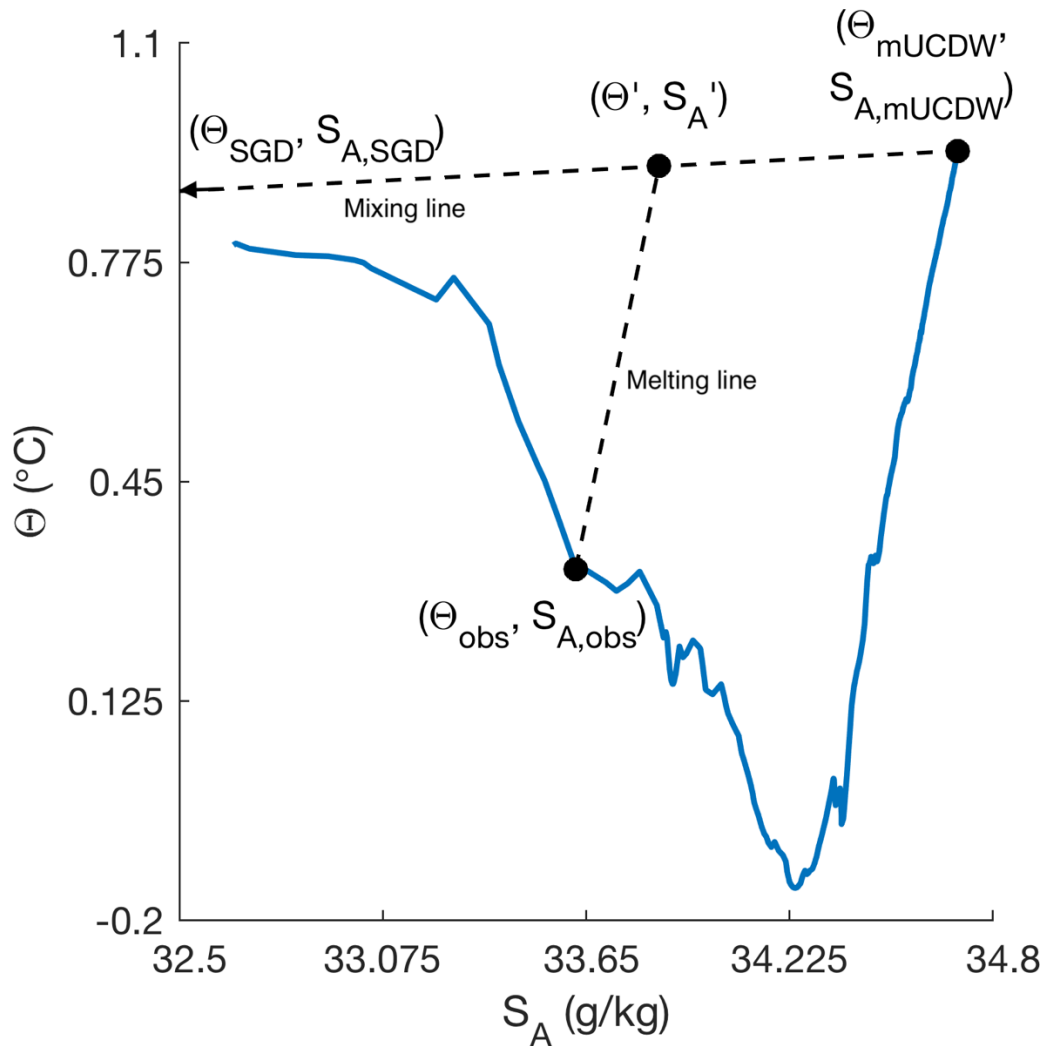
We estimate the ice thickness for key glaciers by using a flux-gate method with surface velocities derived from 15 pairs of 2013-2014 Landsat-8 images. These surface velocities are calculated on a 100 m grid (grid x and grid y directions) with an accuracy of  $\pm 0.05$  m/day and an effective horizontal resolution of 300 m (Fahnestock et al., 2016). Where velocity data were not complete near terminus, we selected the closest upstream transects with complete transect velocity data (noted as “up”). Glacier width along these transects was determined through identifying glacial margins using a combination of visible imagery (rock/ice margins) and velocity gradients (shear margins) from the Landsat-derived velocity data. Where they existed, we use observed fjord depth from multibeam to confirm our ice-thickness estimates were reasonable.

## 2 Supplementary Figures and Tables

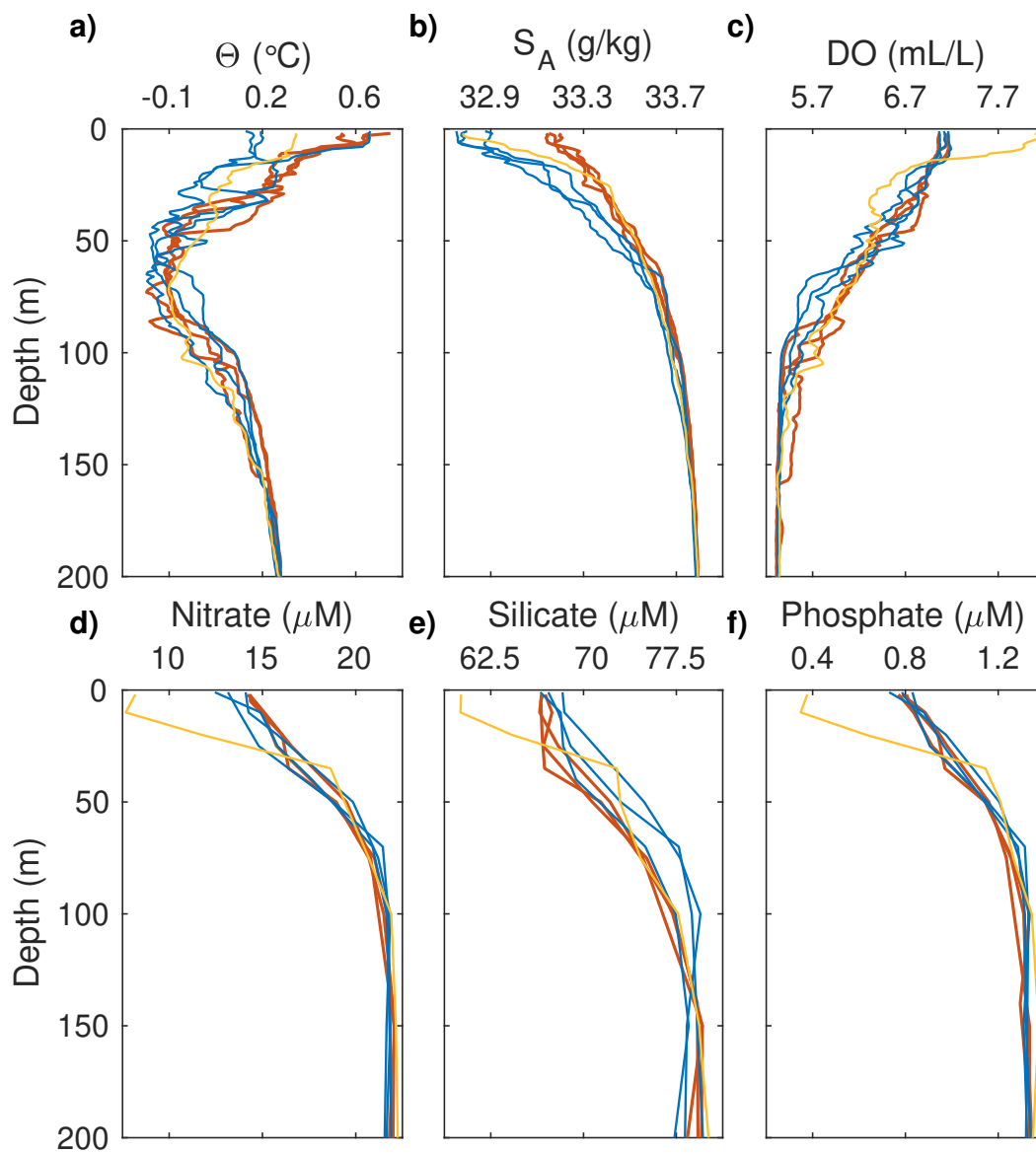
### 2.1 Supplementary Figures



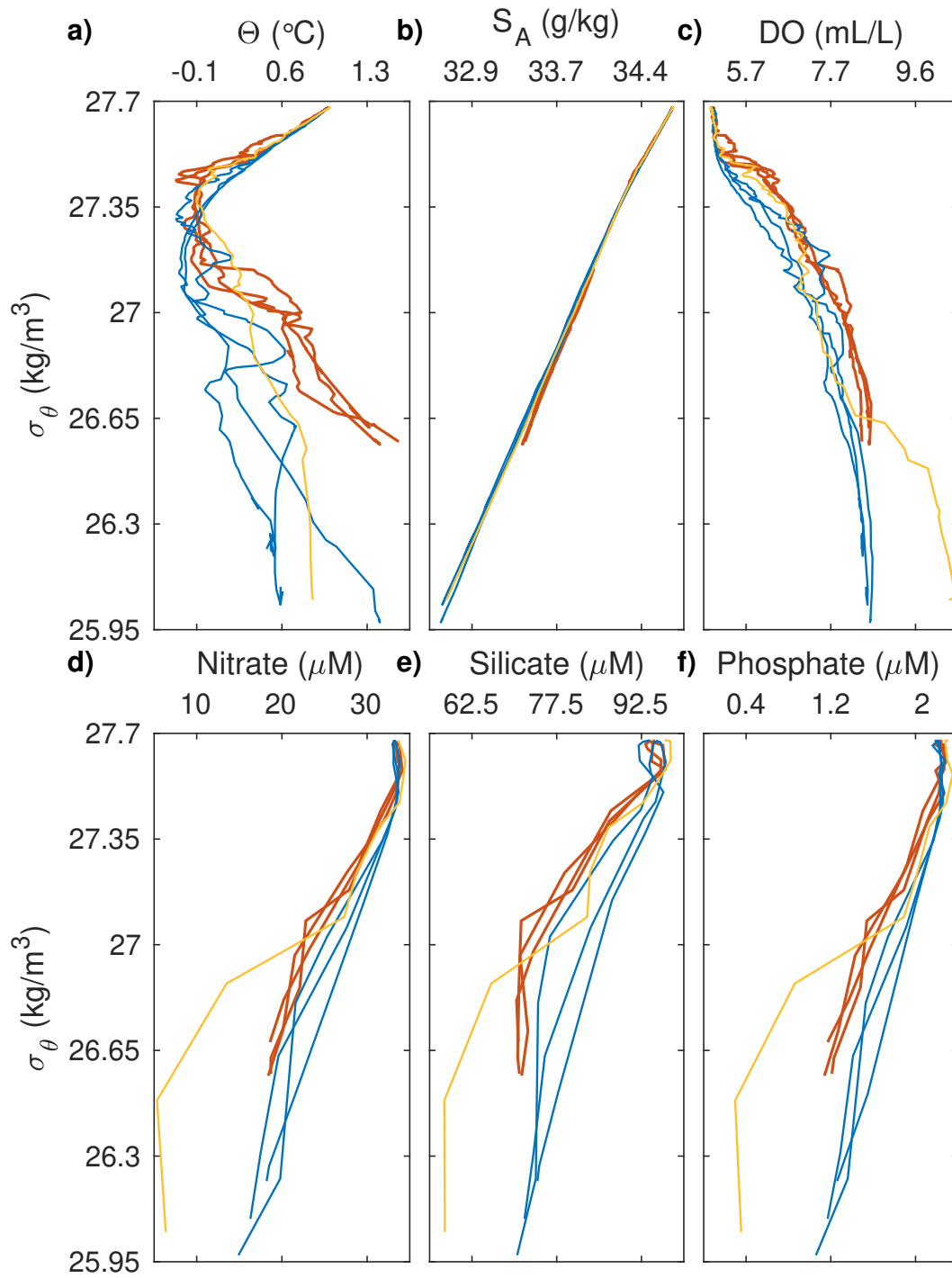
**Supplementary Figure 1:** Seasonal temperature variations within Barilari Bay. Black line shows daily temperature derived from AMPS for the 2009-2010 season, while grey lines show monthly mean temperature for the period 1979-2010 derived from ECMWF ERA-Interim reanalysis.



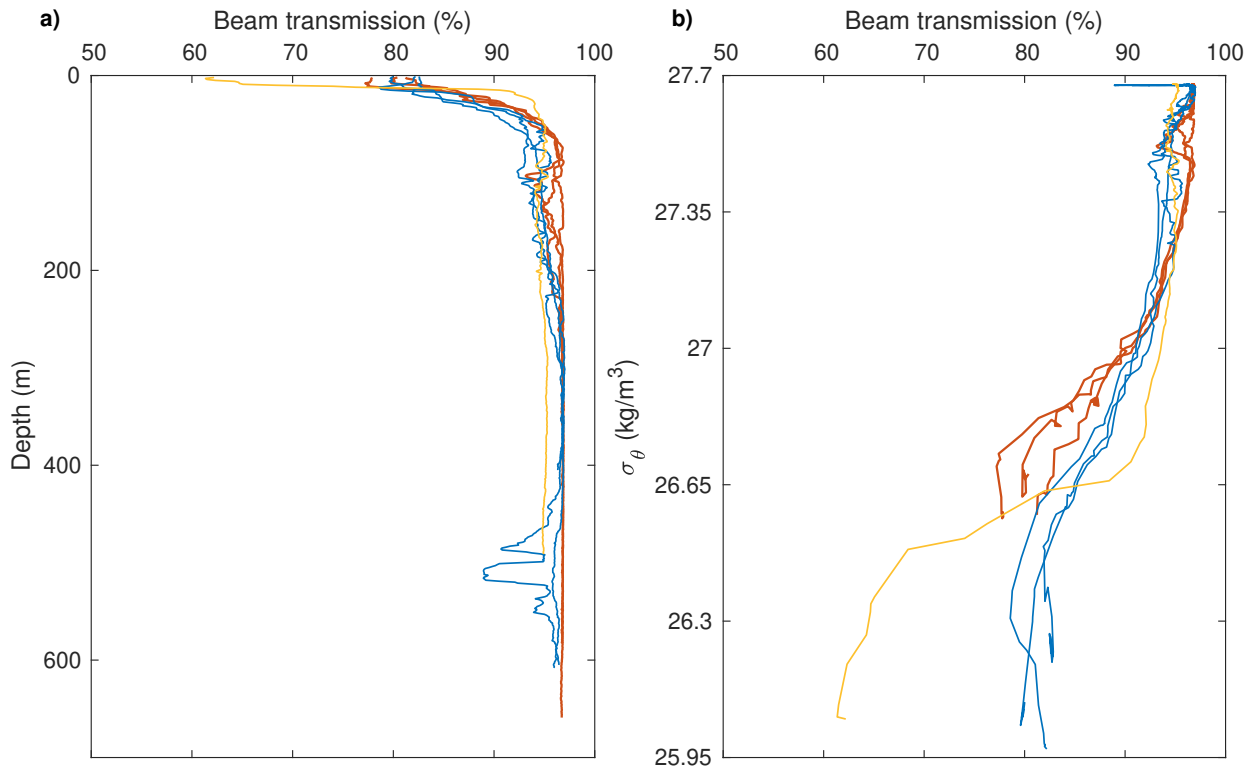
**Supplementary Figure 2:** Diagram detailing changes in ambient water mass properties arising from submarine melting and mixing with subglacial discharge in the framework of the Mor13 model. Observed temperature and salinity properties of a parcel of water ( $\Theta_{obs}, S_{A,obs}$ ) result from the mixing of mUCDW, with properties ( $\Theta_{mUCDW'}, S_{A,mUCDW'}$ ), with subglacial discharge ( $\Theta_{SGD}, S_{A,SGD}$ ), yielding a mixed water mass with properties ( $\Theta', S_A'$ ), alongside thermodynamic changes resulting from melting of glacial ice. Figure reproduced from Mortensen et al. (2013).



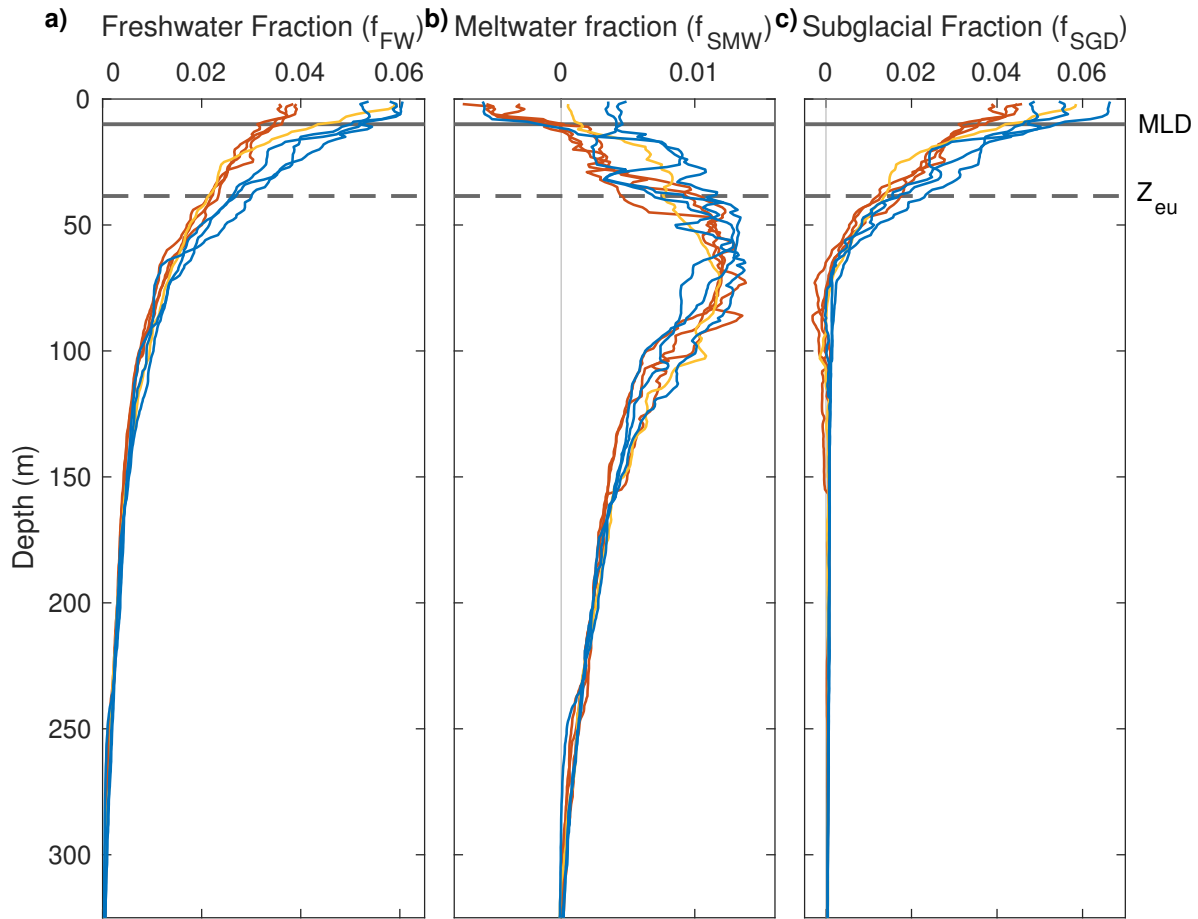
**Supplementary Figure 3:** Same as Fig 3a-f for the top 200 m of the water column.



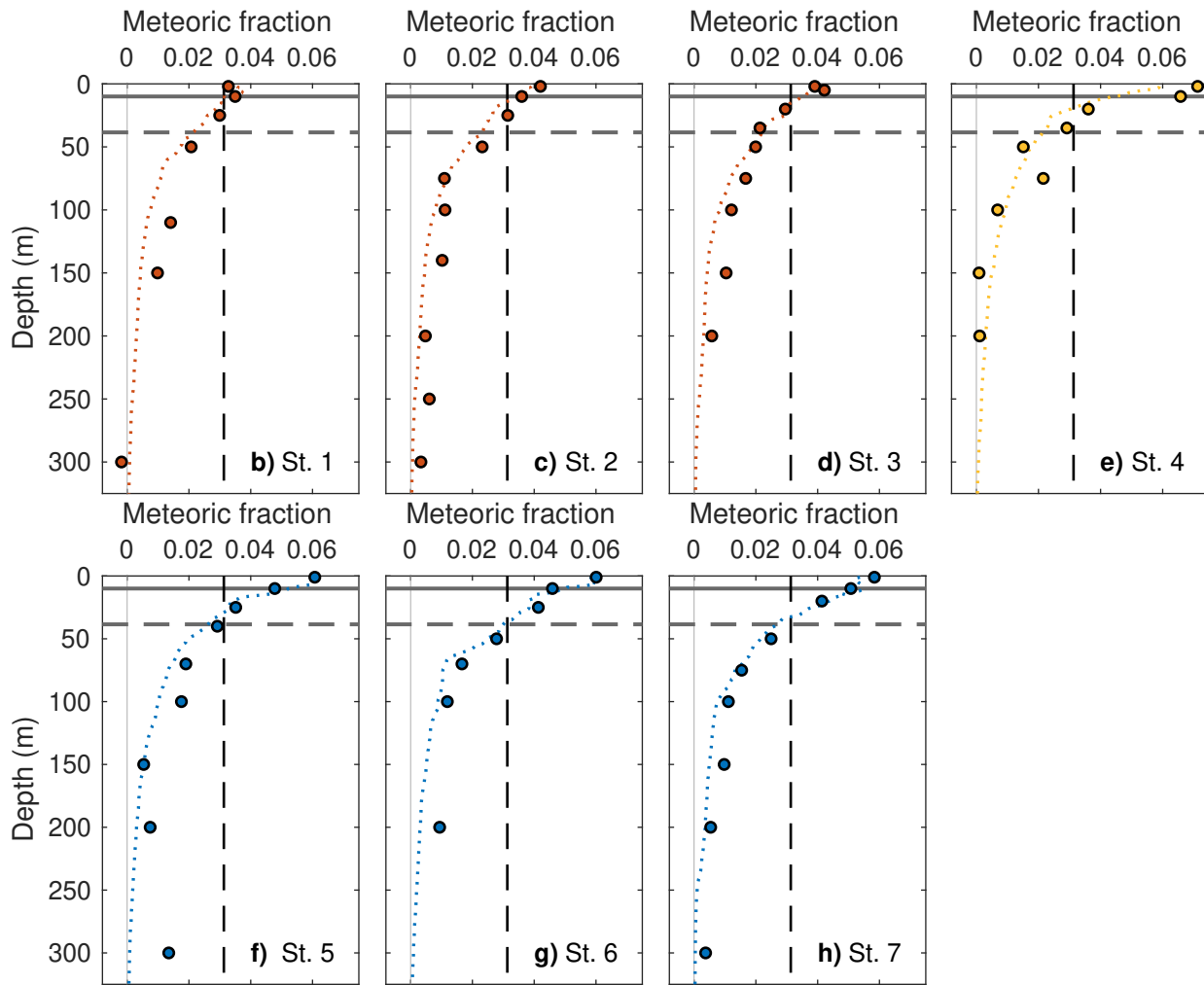
**Supplementary Figure 4:** Same as Fig 3a-f with properties plotted against density.



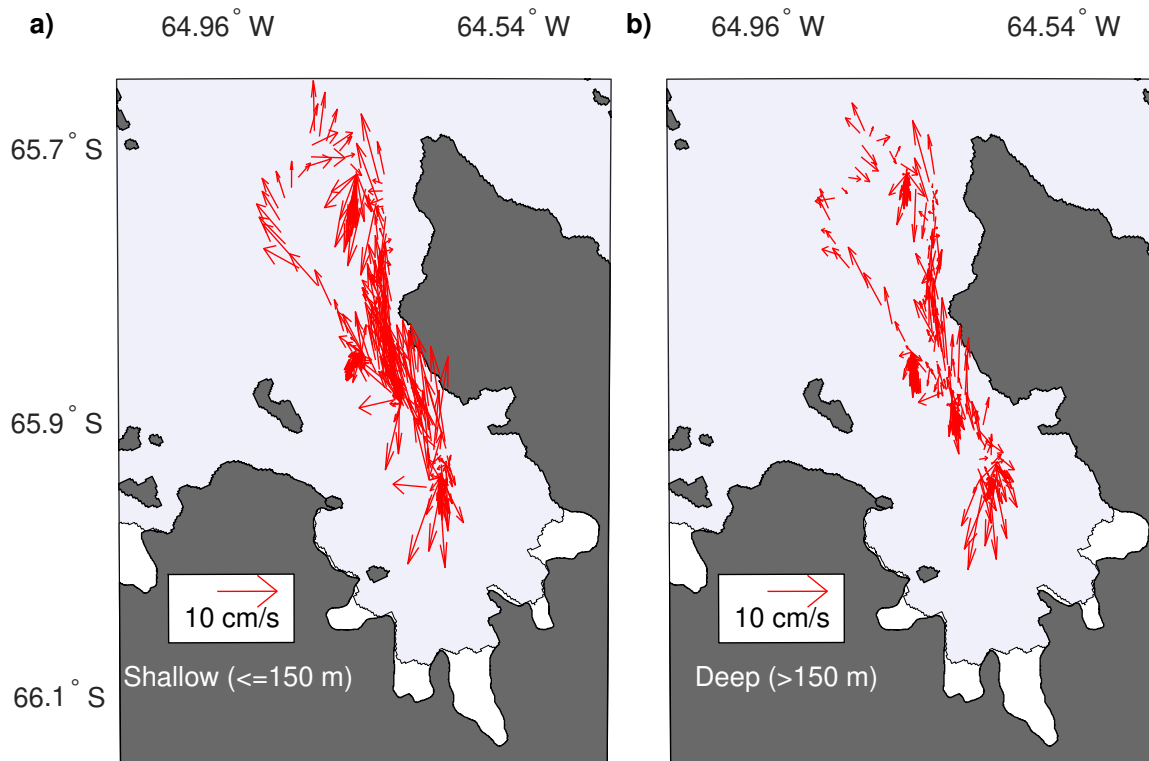
**Supplementary Figure 5:** Water column beam transmission plotted against **a)** depth and **b)** density.



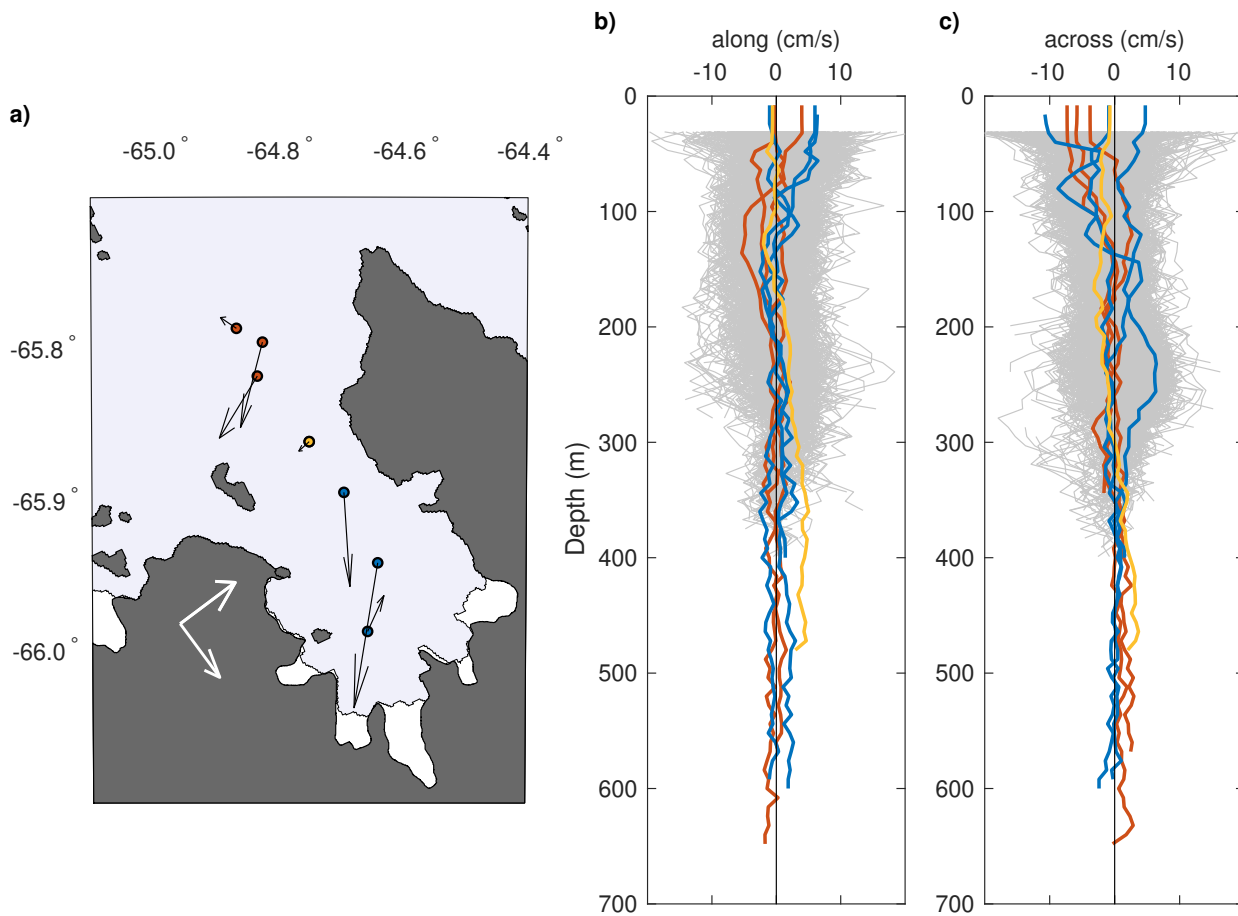
**Supplementary Figure 6:** Mor11 model output showing profiles of **a)** freshwater fraction, **b)** meltwater fraction, and **c)** subglacial fraction. Horizontal dashed line indicates the euphotic zone depth, and the solid horizontal line indicated the mixed layer depth.



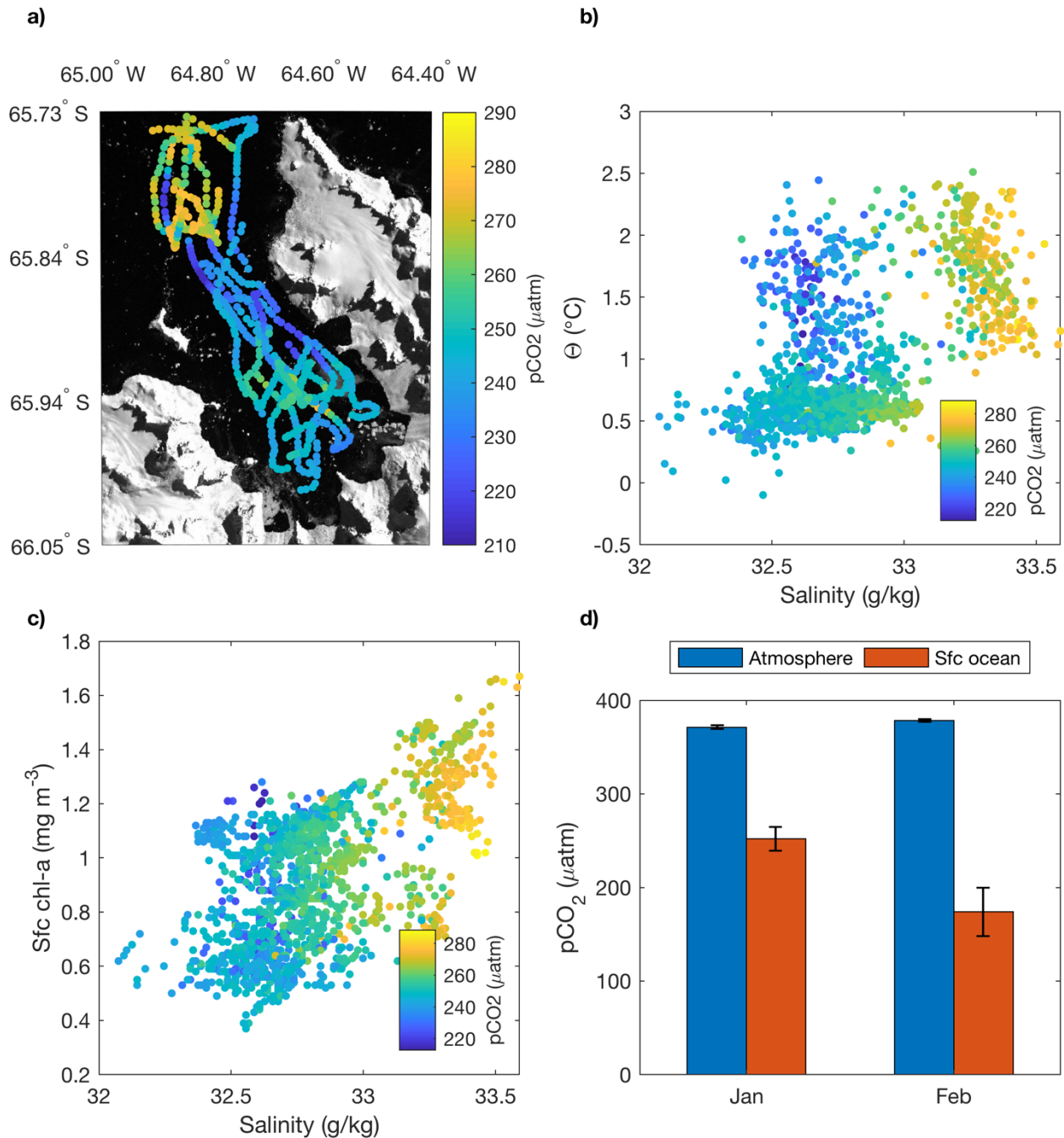
**Supplementary Figure 7:** Meteoric water fraction (glacial meltwater + precipitation) for individual stations, with estimates derived from Mor11 (dashed line) and Mer08 (points). Horizontal dashed line indicates the euphotic zone depth, and the solid horizontal line indicated the mixed layer depth. Dashed vertical line indicates the theoretical upper bound on meltwater fraction (Supplementary equation (11)).



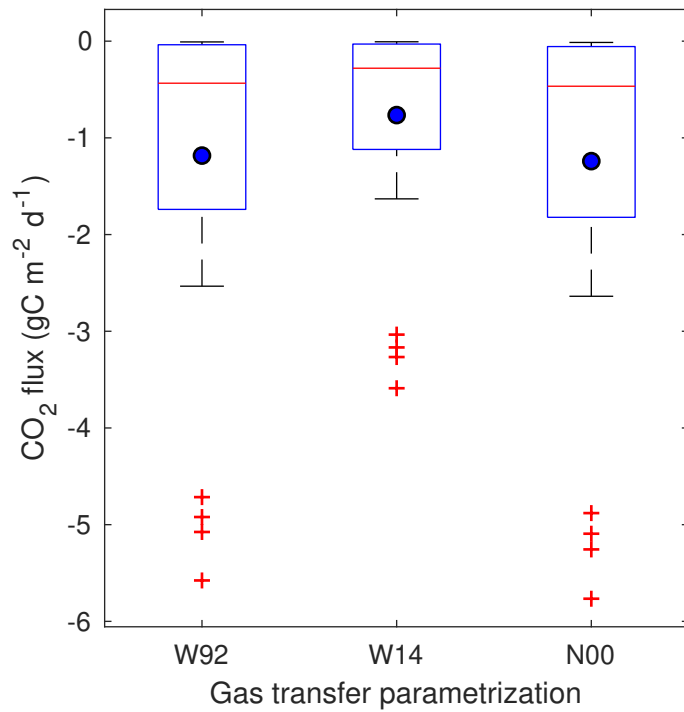
**Supplementary Figure 8:** Same as Fig 7 for February.



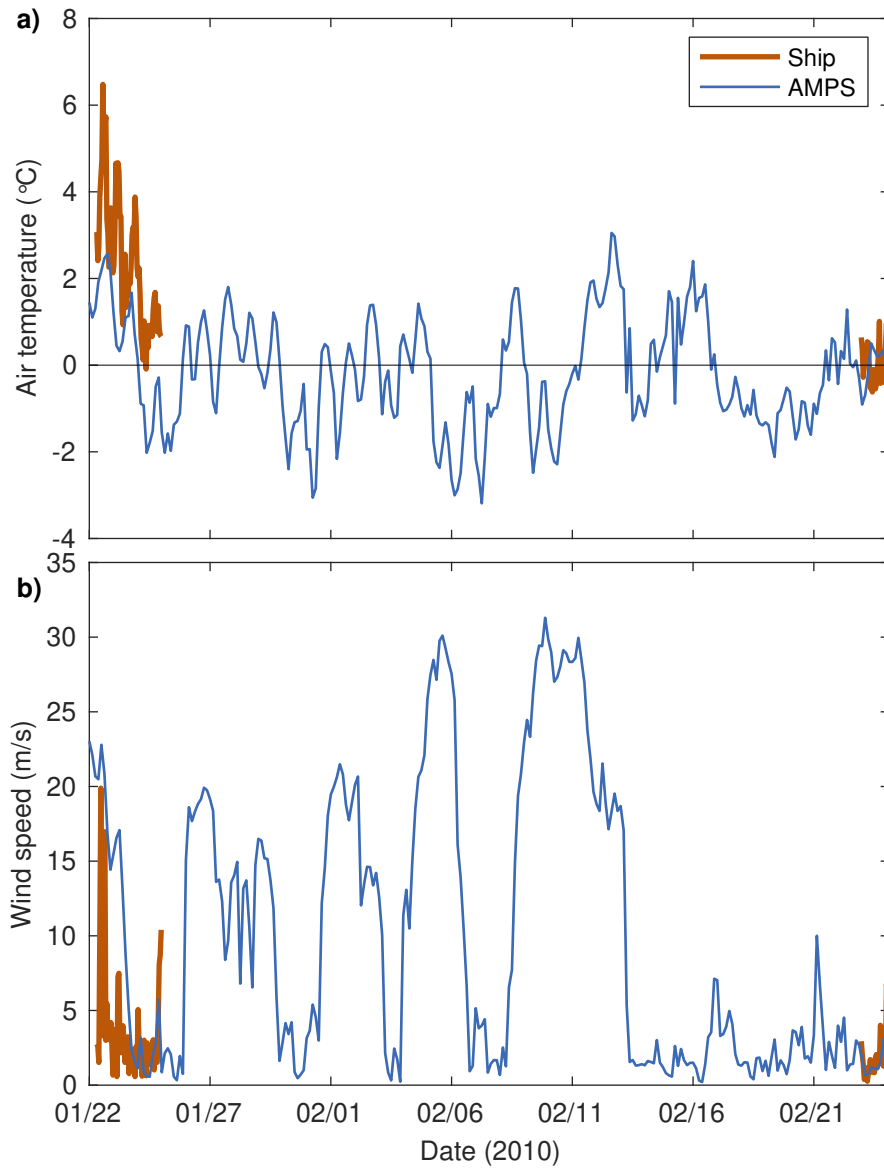
**Supplementary Figure 9:** a) LADCP-derived current vectors averaged over the top 150 m of the water column. Profiles of b) along- and c) across-fjord velocity components. Grey profiles show velocity profiles derived from shipboard ADCP.



**Supplementary Figure 10: a)** Along-track pCO<sub>2</sub> measured in January from the seawater intake. **b)** Temperature-salinity plot with color shading indicating along-track pCO<sub>2</sub>. **c)** Same as b) for chl-a - salinity. **d)** Mean surface ocean and atmosphere pCO<sub>2</sub> concentrations for January and February, averaged over inner fjord waters (i.e. inshore of station 4). Error bars denote one standard deviation about the mean.



**Supplementary Figure 11:** Box plot of daily CO<sub>2</sub> fluxes within the fjord for three different gas transfer parameterization. Red line denotes the median, blue points the mean, and the blue horizontal lines the 25<sup>th</sup> and 75<sup>th</sup> quartile. Outliers are denoted by red crosses.



**Supplementary Figure 12:** Comparison of model (AMPS) and shipboard **a)** atmospheric temperature and **b)** wind speed.

## 2.2 Supplementary Tables

**Supplementary Table 1:** Endmember water mass properties used in the derivation of glacial meltwater distribution in Mor13, Jen99, and Mer08.

Water mass endmember	$\Theta$ (°C)	$S_A$ (g/kg)	DO (ml/kg)	$\delta^{18}O$ (‰)	Source
mUCDW	0.91	34.69	4.71	-0.03	this study
WW	-0.17	34.31	6.19	-0.27	this study
sea ice melt (sim)	N/A	7	N/A	2.1	Meredith et al. (2008)
submarine meltwater (SMW) / meteoric water (met)	-89	0	24	-13.51*	Jenkins et al. (1999) / *this study

### 3 References

Armstrong, F. A. J. (1963). Determination of Nitrate in Water Ultraviolet Spectrophotometry. *Anal Chem* 35, 1292–1294. doi:10.1021/ac60202a036.

Atlas, E. L., Gordon, L. I., Hager, S. W., and Park, P. K. (1971). A practical manual for the use of the Technicon Autoanalyzer in seawater nutrient analyses, rev. Oregon State University, Department of Oceanography.

Bernhardt, H., and Wilhelms, A. (1967). The Continuous Determination of Low Level Iron, Soluble Phosphate and Total Phosphate with the Autoanalyzer. *Technicon Symposium* 1.

Cook, A. J., Murray, T., Luckman, A., Vaughan, D. G., and Barrand, N. E. (2012). A new 100-m Digital Elevation Model of the Antarctic Peninsula derived from ASTER Global DEM: methods and accuracy assessment. *Earth System Science Data* 4, 129–142. doi:10.5194/essd-4-129-2012.

Fahnestock, M., Scambos, T., Moon, T., Gardner, A., Haran, T., and Klinger, M. (2016). Rapid large-area mapping of ice flow using Landsat 8. *Remote Sens Environ* 185, 84–94. doi:10.1016/j.rse.2015.11.023.

Gade, H. G. (1979). Melting of Ice in Sea Water: A Primitive Model with Application to the Antarctic Ice Shelf and Icebergs. *Journal of Physical Oceanography* 9, 189–198. doi:10.1175/1520-0485(1979)009<0189:MOIISW>2.0.CO;2.

Haran, T., Bohlander, J., Scambos, T., Painter, T., and Fahnestock, M. (2014). MODIS Mosaic of Antarctica 2008-2009 (MOA2009) Image Map. Boulder, Colorado USA: National Snow and Ice Data Center. doi:10.7265/N5KP8037.

Jenkins, A. (1999). The Impact of Melting Ice on Ocean Waters. *Journal of Physical Oceanography* 29, 2370–2381. doi:doi: 10.1175/1520-0485(1999)029<2370:TIOMIO>2.0.CO;2.

Jenkins, A., and Jacobs, S. (2008). Circulation and melting beneath George VI Ice Shelf, Antarctica. *J Geophys Res-Atmos* 113. doi:10.1029/2007JC004449.

Meredith, M. P., Brandon, M. A., Wallace, M. I., Clarke, A., Leng, M. J., Renfrew, I. A., et al. (2008). Variability in the freshwater balance of northern Marguerite Bay, Antarctic Peninsula: Results from delta O-18. *Deep-Sea Research Part II* 55, 309–322. doi:10.1016/j.dsr2.2007.11.005.

Mortensen, J., Bendtsen, J., Motyka, R. J., Lennert, K., Truffer, M., Fahnestock, M., et al. (2013). On the seasonal freshwater stratification in the proximity of fast-flowing tidewater outlet glaciers in a sub-Arctic sill fjord. *Journal Of Geophysical Research-Oceans* 118, 1382–1395. doi:10.1002/jgrc.20134.

Rahn, G., and Wegter, B. (2009). Secondary (Lab) standard validation for the analysis of  $\delta^{18}\text{O}$  in water samples using the GasBench and IRMS. Method Validation Report, Antarctic & Environmental Isotope Laboratory, Hamilton College, Clinton, NY.

van Wessem, J. M., Reijmer, C. H., Van Den Broeke, M. R., Cook, A. J., van Uft, L. H., Van Meijgaard, E., et al. (2015). Temperature and Wind Climate of the Antarctic Peninsula as Simulated by a High-Resolution Regional Atmospheric Climate Model. *J of Climate* 28, 7306–7326. doi:10.1175/JCLI-D-15-0060.1.

Xiaolan, W., and Jezek, C. K. (2004). Antarctic ice-sheet balance velocities from merged point and vector data. *J Glaciol* 50, 219–230. doi:10.3189/172756504781830042.